AGU PUBLICATIONS

JGR

Journal of Geophysical Research: Solid Earth

RESEARCH ARTICLE
10.1002/2017JB014826

Key Points:
- We perform seismic velocity and attenuation tomographies for the Northern Kyrgyzstan
- We reveal the crustal structure in a contact zone between the stable Kazakh plate and Tien Shan
- We observe interconnection between the "jelly sandwich" and "crème brûlée" types of the crust

Correspondence to:
I. V. Sychev and I. Koulakov,
ilya.sychev@gmail.com;
koulakoviy@ipgg.sbras.ru

Citation:
Sychev, I. V., Koulakov, I., Sycheva, N. A., Koptev, A., Medved, I., El Khrepy, S., & Al-Arifi, N. (2018). Collisional processes in the crust of the northern Tien Shan inferred from velocity and attenuation tomography studies. *Journal of Geophysical Research: Solid Earth*, *123*, 1752–1769. https://doi.org/10.1002/2017JB014826

Received 7 AUG 2017
Accepted 4 FEB 2018
Accepted article online 13 FEB 2018
Published online 26 FEB 2018

Collisional Processes in the Crust of the Northern Tien Shan Inferred From Velocity and Attenuation Tomography Studies

Ilya V. Sychev[1], Ivan Koulakov[1,2], Nailia A. Sycheva[3], Alexander Koptev[4,5], Irina Medved[1,2], Sami El Khrepy[6,7], and Nasir Al-Arifi[6]

[1]Trofimuk Institute of Petroleum Geology and Geophysics SB RAS, Novosibirsk, Russia, [2]Department of Geology and Geophysics, Novosibirsk State University, Novosibirsk, Russia, [3]Research Station of Russian Academy of Science, Bishkek, Kyrgyzstan, [4]Institut des Sciences de la Terre de Paris, Sorbonne Universités, UPMC Université Paris 06, CNRS, Paris, France, [5]Department of Geosciences, University of Tübingen, Tübingen, Germany, [6]Faculty of Sciences, King Saud University, Riyadh, Saudi Arabia, [7]National Research Institute of Astronomy and Geophysics, Helwan, Egypt

Abstract Based on seismic data from existing seismic networks in Kyrgyzstan, we have constructed new crustal models of seismic velocity and attenuation for *P* and *S* wave s beneath the Kyrgyz Tien Shan. With data from more than 6,000 events recorded by the international KNET network, the most detailed structures were detected in the central-northern part of the study region, where the Kazakh Shield collides with the northern Tien Shan. The independently computed 3-D distributions of *P* and *S* wave attenuation show features that are consistent with the main structural elements. The high-attenuation areas correspond to folded areas of the northern Tien Shan, whereas the partitions of the stable Kazakh Shield and the Issyk Kul block match with the low-attenuation areas. The velocity model reveals some structures that help to determine the details of the collision processes in the northern Tien Shan. In the upper crust, we observe the alternation of several higher- and lower-velocity anomalies that likely represent the interaction of brittle and ductile crustal layers of the collided Kazakh and Tien Shan plates. In deeper sections, both *P* and *S* wave velocity models show a prominent low-velocity anomaly just beneath the northern boundary of Tien Shan. We propose that this anomaly represents an anomalous crustal thickening at the point of underthrusting of the Kazakh Plate beneath Tien Shan.

1. Introduction

The Tien Shan, a mountain belt in Central Asia, extends approximately 2,500 km in the east-west direction and reaches a width of up to 400 km in its western part (Figure 1). It is considered one of the highest mountain systems in the world that is actively developing today. The Tien Shan folded belt is composed of several parallel mountain chains and intermountain basins and is located at the northernmost margin of the large folded system in Central Asia affected by the collision of India and Asia (inset in Figure 1) (Molnar & Tapponnier, 1975). To the north, it is bounded by the immobile Kazakh Shield, which is part of the stable North Asia assemblage. From the south, the Tien Shan is squeezed by the Tarim Plate, which, in turn, is pushed northward by the compressed Tibetan Plateau. The orogenesis in the Tien Shan region was delayed relative to the beginning of the Indian collision to approximately 30 Myr (Tapponnier & Molnar, 1979). Within the Tien Shan, the initiation of folding showed a trend of gradual development from south to north with a difference of approximately 2–3 Myr (Buslov et al., 2004). Presently, the Tien Shan exhibits horizontal shortening of 20–25 mm/year in the south-north direction (Abdrakhmatov et al., 1996, 2001). This shortening accommodates approximately 40% of the divergent movement of the Indian Plate with respect to the stable parts of the continent, which makes it one of the most rapidly moving elements of the collision belts in Asia (Larson et al., 1999). These active tectonic processes make the Tien Shan one of the most representative examples of ongoing continental collision, and therefore attract the attention of many specialists from around the world.

The Tien Shan is relatively well investigated because of the joint efforts of several international teams working there since the 1990s. The deployment of a considerable number of permanent and portable seismic stations in different periods provided a large amount of data, in addition to information from the seismic network operated by the Geophysical Survey of Kyrgyzstan. These data were used in a number of studies, which

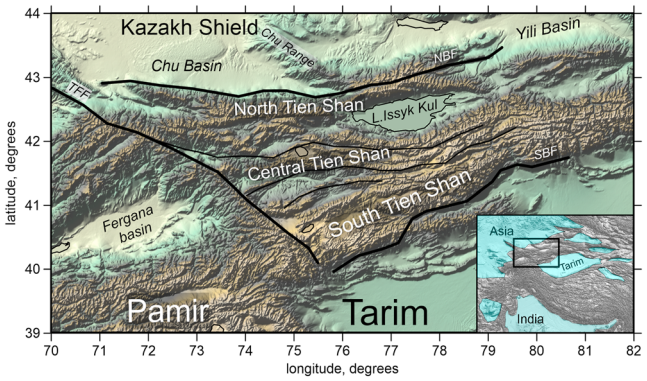

Figure 1. Major structural units in the study region. The black lines are the major faults. TFF, Talas-Fergana Fault; NBF, North-Boundary Fault; SBF, South Boundary Fault. Inset represents the location of the study area in the Central Asian collision belt. The blue areas highlight mechanically rigid lithospheric blocks.

provided information on crustal and mantle structures beneath the Tien Shan. The first tomography model of the crust based on portable network data was constructed by Roecker et al. (1993). Later, the same data were reprocessed by several teams using various tomography techniques (Ghose et al., 1998; Sabitova et al., 1998; Sabitova & Adamova, 2001). More recently, the crustal and uppermost mantle models were updated based on new data and more sophisticated algorithms (Li et al., 2009; Omuralieva et al., 2009; Xu et al., 2007; Zhao et al., 2003). Approximately same data were used in tomography studies of the crust and uppermost mantle beneath the Kyrgyz Tien Shan in Lei (2011) and Zabelina et al. (2013). A regional study of Pn velocities and azimuthal anisotropy beneath the entire Tien Shan belt (including its Chinese part, Tarim, and other surrounding areas) was studied in Zhou and Lei (2015). The surface wave data were jointly inverted together with gravity and receiver function data in Li et al. (2016) for the Kyrgyz Tien Shan and provided robust constraints for the crustal thickness and velocities.

Although numerous studies listed in the previous paragraph have been conducted on the crustal and uppermost mantle structures, the understanding of the actual structures is still far from definitive. Indeed, most of the models in the above-mentioned studies appear to be uncorrelated with each other, and in some cases present contradictory features.

Better consistency has been achieved in studying mantle structures. Teleseismic studies based on data from regional seismic networks were conducted independently by Lei and Zhao (2007) and Xu et al. (2007). They revealed similar features: a northward dipping anomaly, which was interpreted as the subducted Tarim lithosphere, and another dipping anomaly associated with the Kazakh Shield. Similar features were identified in the tomography model for the whole of Asia by Koulakov (2011), which will be further evaluated in section 5 of this paper.

In addition to seismic tomography, several other studies based on other methods provided important information about the deep structure beneath the Tien Shan. Careful analysis of available seismic data using receiver function techniques has provided information on the interfaces in the crust (Kosarev et al., 1993; Vinnik et al., 2004, 2002) and in the upper mantle (Chen et al., 1997; Oreshin et al., 2002; Tian et al., 2010). In the context of this study, it is important to note that Vinnik et al. (2004) found robust evidences for the large crustal thickness (up to 60 km) beneath the northern margin of the Tien Shan at the boundary with the Kazakh Shield. This Moho dipping does not appear to be isostatically compensated by the topography and remains an enigmatic structure. A recent receiver function study by Yu et al. (2017) has provided the shapes of the mantle discontinuities beneath the entire Tien Shan and its surroundings. They linked the observed undulations of these boundaries with sinking of the lithosphere due to the ongoing collision.

To provide a complete overview of previous geophysical studies, several active-source seismic surveys and electromagnetic studies must be mentioned. Deep seismic sounding profiling was first conducted in the Tien Shan in the 1960s (Gamburtsev, 1960) but was then interrupted for decades. Recently, active source seismic studies have been resumed for the MANAS profile, which produced a great deal of information on the deep structure beneath the central and southern Tien Shan using several geophysical methods (Makarov et al., 2010). Mantle and crustal structures beneath the Tien Shan were also investigated using magnetotelluric methods by Bielinski et al. (2003), Batalev et al. (2011), and Batalev and Bataleva (2013), including the MANAS profile (Rybin, 2010).

Information on deep structures derived from various geophysical studies should be a key element for understanding the collisional processes in the Tien Shan and other belts with similar genesis. However, the inconsistencies that exist between the results do not allow determination of unambiguous constraints, and therefore, the interpretation models are sometimes speculative and contradictory. In this study, we present another tomography model for the crustal structure beneath the Kyrgyz Tien Shan that includes the distributions of both seismic velocities and attenuation of *P* and *S* waves. With newly added data and careful testing,

we have achieved improvements relative to most previous models. Our results allow us to make clear tectonic interpretations, which are presented in section 5.

2. Data and Algorithms for Velocity Tomography

To build the models of seismic velocities, we used arrival times of the *P* and *S* waves from local events in the Tien Shan region recorded by stations in Kyrgyzstan and the surrounding countries. The data set was composed of two parts. The first part was provided by the Institute of Seismology of the National Academy of Science of Kyrgyzstan. This data set was based on existing permanent stations across the entire area of Kyrgyzstan and included the traveltimes of 6,175 *P* waves and 4,988 *S* waves from 435 earthquakes (25.6 picks per event on average). This data set was previously used by Zabelina et al. (2013) to build the crustal tomography model of Kyrgyzstan.

The second subset included data from the time period of 1999 to 2014 recorded by the KNET network, which is the first regional continuous telemetric network composed of 10 broadband seismic stations in Kyrgyzstan. It was installed in 1991 by several institutions under the Joint Seismic Program by the Incorporated Research Institutions for Seismology, and it has successfully operated up to the present. This subset included the data for more than 6,000 local events; however, it enabled much smaller ratios of picks per event compared with the first part of the data set, and it mainly covered the central-northern part of Kyrgyzstan. The waveform data corresponding to this network were also analyzed to estimate the attenuation parameters (t^*), which were then used to derive the three-dimensional distribution of seismic attenuation. Details on the attenuation tomography workflow will be presented in the next section.

Note that for the area of Kyrgyzstan, a few other temporary seismic networks were installed in previous years. For example, a large TIPAGE network, which operated in 2008–2010, covered Tajikistan and a southern part of Kyrgyzstan. However, as we are mostly interested in the northern part of Tien Shan that was not covered by the TIPAGE network, these data were not included into our tomographic inversions.

For velocity tomography, we selected data with total numbers of *P* and *S* picks per event equal to or larger than 10. During the preliminary location procedure, we removed picks with absolute deviations of more than 1 and 1.5 s for *P* and *S* wave s, respectively. No other selection criteria were applied. In total, we used 34,676 *P* and 27,345 *S* wave picks from 4,775 events (almost 13 picks per event) for the tomography. The ray coverage corresponding to the tomography inversion is shown in Figure 2a.

The arrival times of the *P* and *S* waves were inverted to three-dimensional models of the *P* and *S* velocities and locations of the events using the iterative code LOTOS (Koulakov, 2009) for passive-source tomography. The calculations start from the preliminary source locations using a very stable grid-search method that enables finding the solution for the source even if no a priori information on the source coordinates is known. To make the calculations at this step more efficient, we used an approximate algorithm for calculations of traveltimes based on interpolation of tabulated values for different depths and epicentral distances calculated at a preliminary step.

The iterative procedure of tomographic inversion starts with the re-location of sources using the updated three-dimensional models of the *P* and *S* velocities. At this step, we used the gradient method of optimization, which makes faster calculations of the most probable source location. Traveltimes were computed using the 3-D ray tracer based on the principle of time minimization (bending algorithms) proposed by Um and Thurber (1987).

The raypaths obtained after location in the first iteration were used to build the parameterization grid. We installed the nodes of the grid only in areas with sufficient amounts of data (Figure 3). In the map view, the grid nodes are regularly spaced (10 km spacing in our case). In the vertical direction, spacing depends on ray density but cannot be smaller than a predefined value (3 km in our case). We computed the results using several grids with different basic azimuths (four grids with orientations of 0, 22, 45, and 67°). Averaging results obtained in this way allowed us to minimize any artifacts of grid geometry. Note that the grids are installed only in the first iterations. In the next iterations, the velocity values are updated in the same nodes.

Inversion is performed simultaneously for the *P* and *S* velocity anomalies, corrections for source coordinates and origin times, and station corrections. In our case, the station correction term appeared to be important. In the previous study by Zabelina et al. (2013), there were prominent shallow anomalies around some stations.

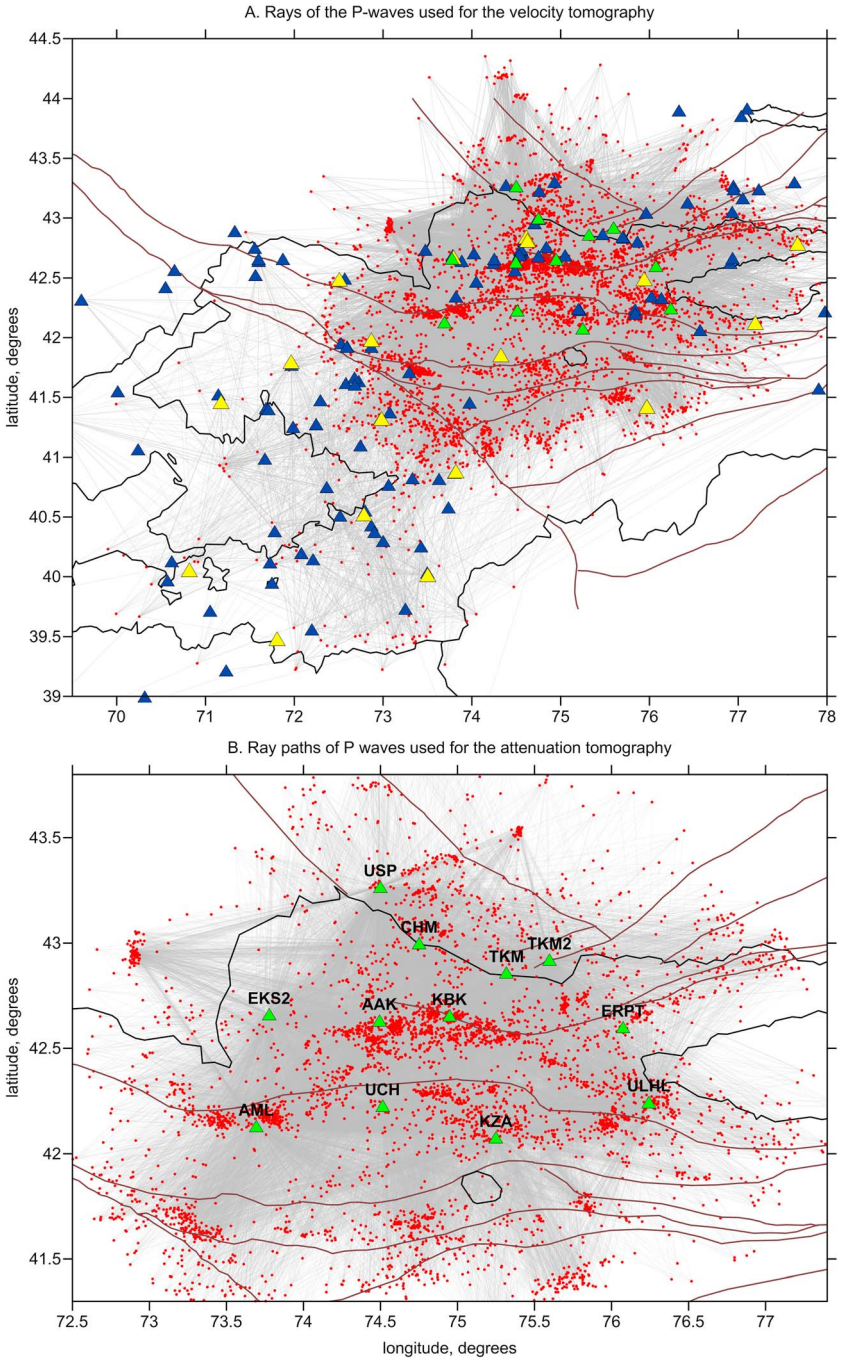

Figure 2. The distributions of data in tomography studies for (a) velocity and (b) attenuation. The green triangle depicts KNET, the yellow triangle depicts KRNET, the blue triangles depict other seismic stations, and the red dots are the earthquakes. The grey lines represent the paths of the *P* rays. For the *S* wave data, the ray configurations are similar. In b, the violet lines represents the major faults.

In this case, after defining nonzero weights for the station corrections, these anomalies disappeared completely. The inversion on the large sparse matrix was performed using the LSQR algorithm by Paige and Saunders (1982) and Nolet (1987). The stability of the inversion was controlled by amplitude damping and flattening, which minimized the differences of solutions in neighboring nodes. The main system of linear equations can be presented as

$$A_{ij}dVP_j + B_{ik}dVS_k + C_{il}X_l = dtj \;\; j = 1\ldots NP; k = 1\ldots NS; l = 1\ldots 4, \quad (1)$$

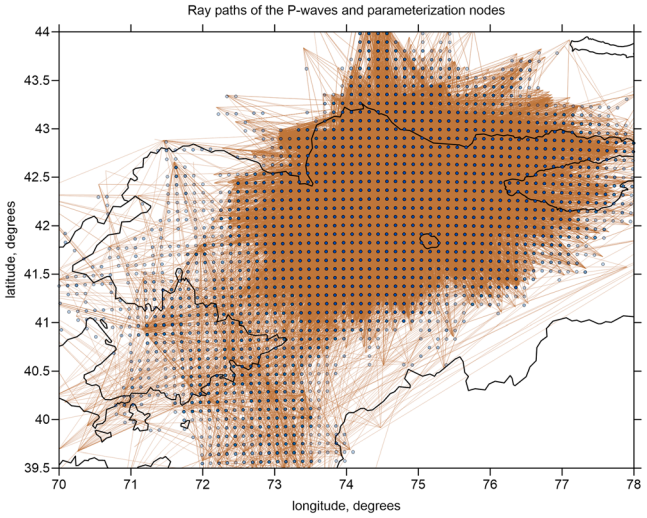

Figure 3. Construction of the parameterization grid for the velocity inversion. The brown lines depict the *P* raypaths. The dots are the locations of the parameterization nodes. The intensity of the dot color represents the number of nodes on each of the vertical lines.

where *dVP* and *dVS* are the *P* and *S* wave velocity parameters with the corresponding numbers *NP* and *NS*; *A* and *B* are the first derivative matrices for the *P* and *S* parameters, respectively; *X* represents source parameters (coordinates and origin times); and *i* is the number of rays. Amplitude damping is realized by adding supplementary equations:

$$WP^{am} dVP_j = 0 \quad j = 1 \ldots NP; \tag{2.1}$$

$$WS^{am} dVS_j = 0 \quad k = 1 \ldots NS; \tag{2.2}$$

where WP^{am} and WS^{am} are the amplitude damping coefficients (the larger they are, the smaller the amplitudes of anomalies become). The flattening of the resulting velocity models is performed by adding another group of equations:

$$WP^{sm}(dVP_m - dVP_n) = 0 \tag{3.1}$$

$$WS^{sm}(dVS_m - dVS_n) = 0 \tag{3.2}$$

where *m* and *n* are the numbers of nodes corresponding to all pairs of neighboring nodes and WP^{sm} and WS^{sm} are the flattening coefficients (the larger they are, the smoother the resulting models become).

The coefficients for the amplitude damping and flattening were estimated using several trials of inversions with experimental and synthetic data. In our workflow, we prefer fixing the total number of iterations (three in our case) and then tuning the amplitude and flattening to obtain the optimal solution.

The optimal reference 1-D model was estimated after several runs of the full inversion. In the first run, we used the starting model from the previous study (Zabelina et al., 2013). After completing the full iterative inversion procedure, we computed average values of the *P* and *S* velocities at certain depths. We then used these values for the next run of full calculations. After several consequent runs, we obtained the optimal reference model presented in Table 1, which provided balanced positive and negative anomalies in the resulting tomography. The velocity values in the reference 1-D model are defined at some depth levels and linearly interpolated between. Note that we do not define sharp interfaces, such as the Moho, to avoid artificial horizontal structures in the final velocity model. Although the structures in the study area are expected to be strongly heterogeneous, we do not support an idea to impose the existing knowledge on the geological structures into the starting model. After performing the tomography inversion, we prefer obtaining independent confirmation of the existing information on significant Moho depth undulations, derived from independent studies (e.g., from receiver function studies by Vinnik et al., 2004).

The values of the residual deviations in L1 norm and variance reductions are given in Table 2. Note that aside from the generally lower accuracy of *S* wave picking, the reduction of the *S* wave residuals is much higher and reaches almost 60%. This finding can be explained by stronger amplitudes of the *S* anomalies and higher sensitivity of the *S* wave data. The final deviations of 0.2 and 0.3 s for the *P* and *S* wave data, respectively, are close to the picking accuracy estimates.

Table 1
The 1-D Velocity Distributions Used as a Starting Model for Tomography

Depth (km)	V_P (km/s)	V_S (km/s)
−1	5.5	3.0
15	6.0	3.3
35	6.5	3.5
55	7.4	4.1
120	8.0	4.5

3. Attenuation Tomography

To study the 3-D distributions of seismic attenuation, we used the algorithm described by Sychev et al. (2017) for the case of a much smaller region of Harrat Lunayir in Saudi Arabia. Here we only briefly describe the major steps used to analyze the data and to perform the inversion. The input data for the attenuation tomography were estimated using the spectral inversion algorithm proposed by Haberland and Rietbrock (2001) and Rietbrock (2001). It is based on consideration of the signal spectrum, and for the *i*th source recorded by the *j*th receiver it can be presented as

$$A_{ij}(f) = S_i(f) I_j(f) G(s) \exp\left(-\pi f \frac{t_{ij}}{Q_{ij}}\right), \tag{4}$$

Table 2
Deviations of the P and S Wave Residuals (in the L1 Norm) and Their Reduction During Inversion of Experimental Data

Iteration	*P* residual deviation (s)	*P* residual reduction (%)	*S* residual deviation (s)	*S* residual reduction (%)
1	0.336	0	0.706	0
2	0.246	26.6	0.367	47.9
3	0.216	35.6	0.292	58.5

where f is the frequency, $I_j(f)$ is the instrument term, $G(s)$ is the geometrical spreading, Q_{ij} is the quality factor, t_{ij} is the traveltime of the seismic wave between the source and receiver, and $S_i(f)$ is the source spectrum, which can be approximated using the Brune model (Brune, 1970) as

$$S_i(f) = \frac{\Omega_0}{1 + \left(\frac{f^2}{f_c^2}\right)}, \tag{5}$$

where f_c is the corner frequency and Ω_0 is the low-frequency spectral plateau containing frequency-independent parts.

For tomography, we used the value of t^*:

$$t_{ij}{}^* = t_{ij} Q_{ij}{}^{-1}. \tag{6}$$

In a heterogeneous medium, the total energy loss due to attenuation along the raypath can be presented as an integral:

$$t_{ij}{}^* = \int_{\text{path}} \frac{ds}{Q(s)v(s)}, \tag{7}$$

where $v(s)$ is the velocity of the seismic wave along the raypath s.

Using (2.1) and (2.2) and (3.1) and (3.2), the signal spectrum in (4) can be presented as follows:

$$A_{ij}(f) = \frac{\Omega_{0ij} \exp\left(-\pi f t_{ij}{}^*\right)}{1 + \left(\frac{f^2}{f_c^2}\right)}, \tag{8}$$

where Ω_{0ij} contains the frequency-independent terms, including the geometrical spreading.

Using the grid search method, we optimized the values of f_c, $t_{ij}{}^*$, and Ω_{0ij} in (8) to achieve the best fit between the computed and observed spectra of the signal. To estimate the quality of the t^* determination, we optimized for both the relevant seismic wave and noise. Figure 4 presents examples of spectral analysis of the *P* and *S* wave arrivals and that of the background noise, which were used to derive the t^* data used in this study. If the signal-to-noise ratio was less than 3, or if the spectral curves of the signal and noise crossed each other, such data were excluded from the consideration.

We performed independent analyses for the arrivals of *P* and *S* waves. In both cases, we used a window of 2.5 s just after the picking time. To compute the noise spectra, we used the same interval, but corresponding to the time prior to wave arrival. As a result of this analysis, we have calculated 12,409 and 13,786 values of t^* for *P* and *S* data, respectively, which were used as input for tomography inversion. The rays corresponding to these data are presented in Figure 2b.

The tomography inversion for the inversion employed the algorithm that was previously used in other attenuation studies (Koulakov et al., 2010; Sychev et al., 2017). It uses the same instruments for model parameterization and inversion as in the LOTOS code, but the calculations are performed within one iteration without updating the source coordinates. Similar to the case of calculation of the velocity model, in the attenuation tomography, we used several parameterization grids with different orientations and then averaged the results. For calculation of attenuation, we use the velocity models, raypaths, and source coordinates obtained after iterative velocity tomography. As a result of tomographic inversion, we computed the deviations of attenuation ($A = 1/Q$) relative to their average values.

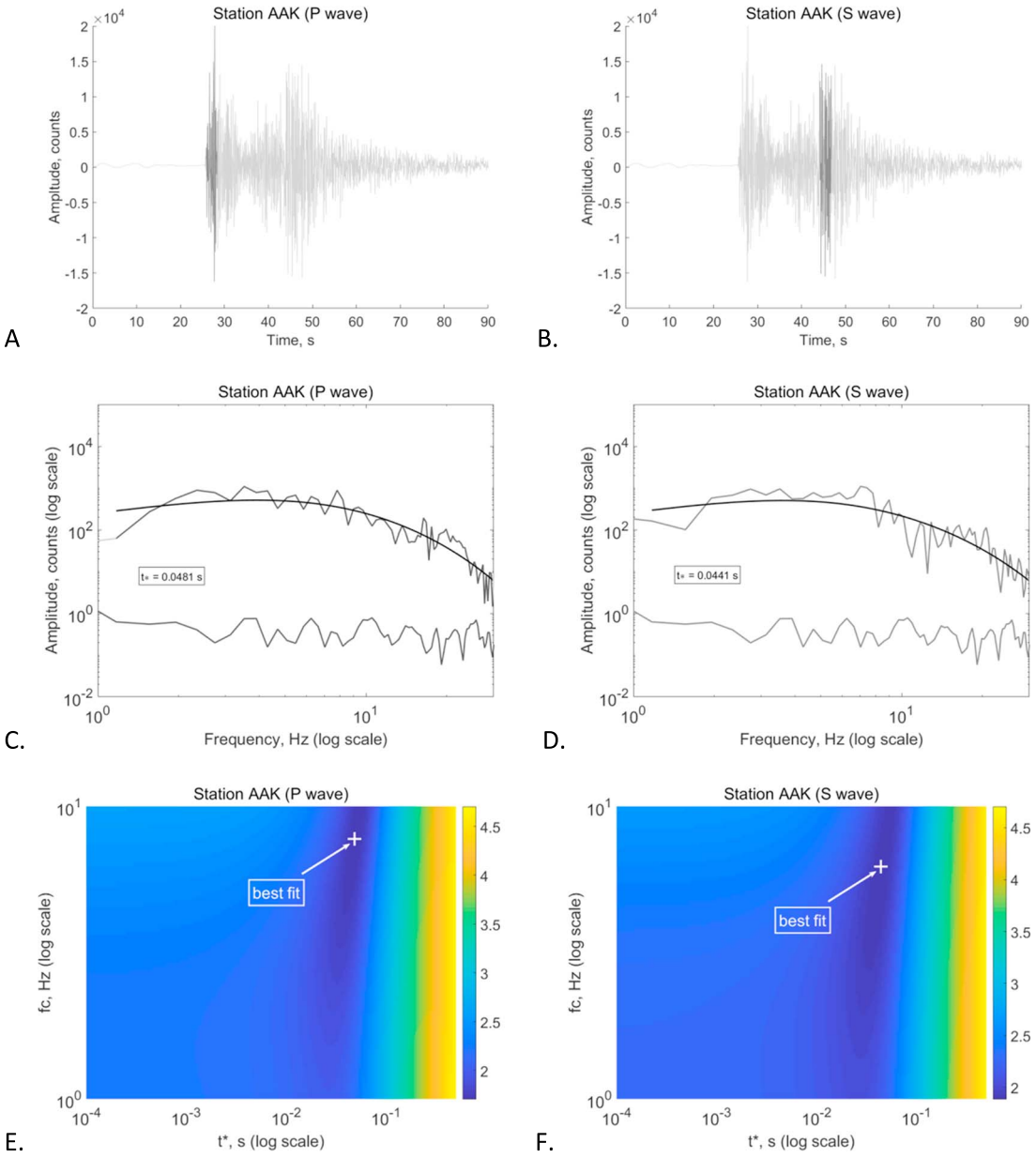

Figure 4. Workflow for calculating the *t** for the *P* and *S* waves. (a and b) Parts of seismograms (darker grey) used for picking *t** for the *P* and *S* data, respectively. (c and d) Examples of the noise and signal spectra for the *P* and *S* arrivals (lighter lines). The solid darker lines indicate the modeled spectra based on optimal values of parameters. (e and f) Examples of the grid search optimization results for the best values of *t** and fc for the *P* and *S* waves. The colors indicate the misfit between the observed and modeled spectra.

To compute attenuation, we only used KNET data with rays with limited epicentral distances and depth penetrations. For this reason, the model cannot be resolved below 15 km depth. The resolution area in the resulting maps appears wider than the network aperture because for attenuation tomography, we used data recorded from earthquakes that occurred outside the study area. Note that in the case of studying attenuation, the role of source uncertainty is less dramatic than it is during joint tomography for velocity and source parameters.

It should be noted that the 3-D velocity model was used in the calculation of attenuation and can therefore affect it in some way. To assess this effect, we performed several inversions for attenuation using different velocity models (including the 1-D velocity structure) and obtained generally identical structures.

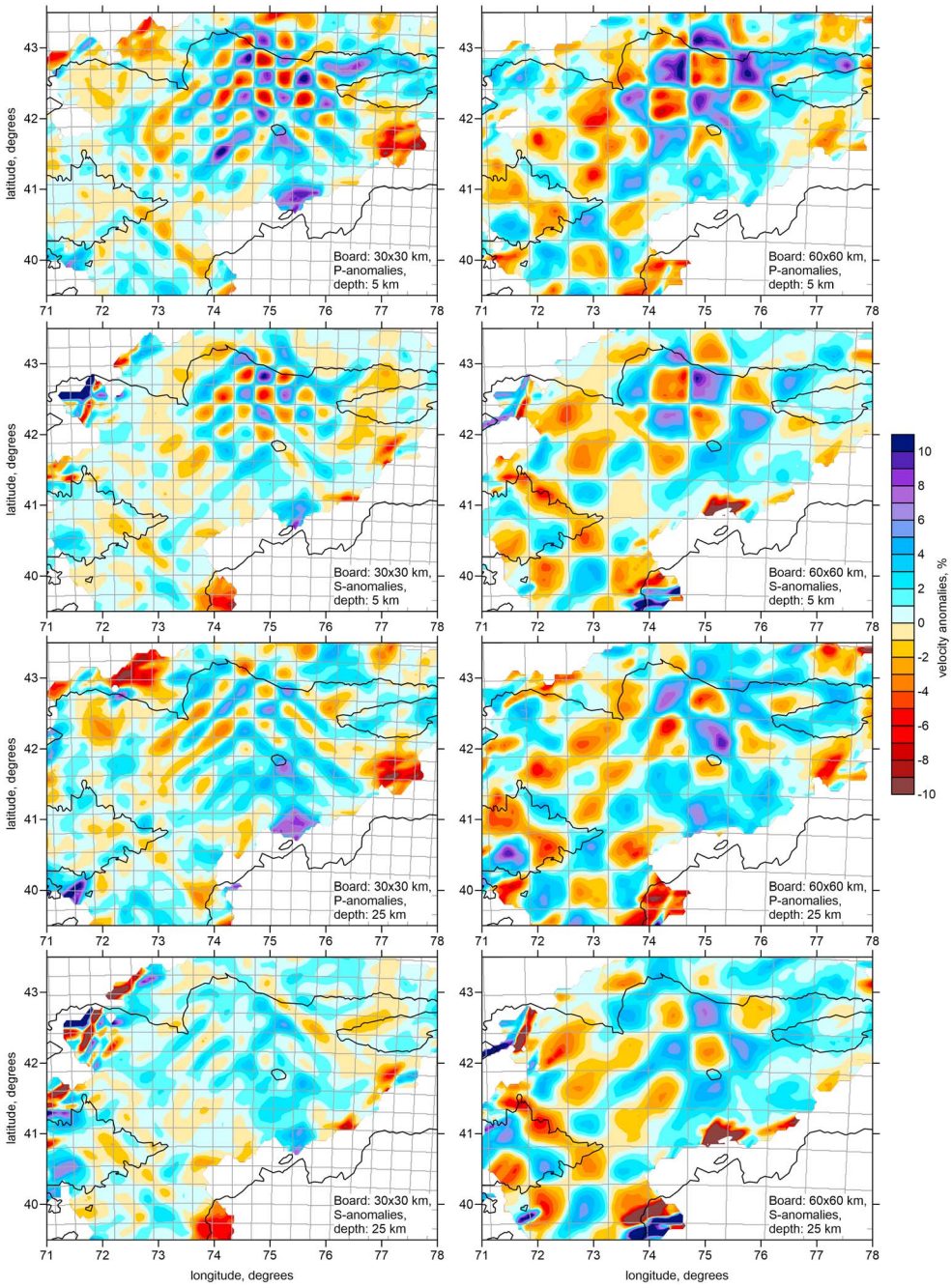

Figure 5. Checkerboard tests for two models shown for the *P* and *S* wave velocity anomalies at the depths of 5 and 25 km. The grey lines highlight the shapes of the initial anomalies.

4. Testing

Before discussing the main results of our experimental data analysis, we present several synthetic tests for the velocity models. Synthetic modeling is an important stage in tomography studies not only because it provides estimates for the resolution and reliability of the recovered model but also because it helps to determine the optimal values of free parameters, such as grid spacing, damping, and smoothing. Synthetic modeling should simulate the workflow of the real tomography experiment as closely as possible. In the case of synthetic modeling, we used the same source-receiver pairs as those in the experimental data set. The three-dimensional synthetic model was defined independently of the parameterization used for inversion.

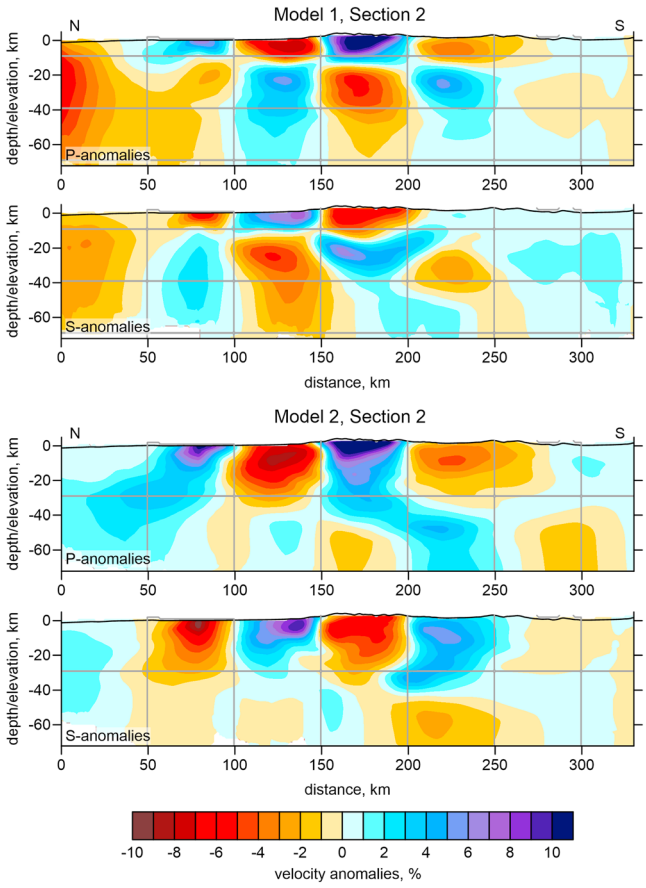

Figure 6. Tests for checking the vertical resolution using two checkerboard models defined in vertical section 2 (See Figure 7). The grey lines highlight the shapes of the initial anomalies.

The synthetic traveltimes were calculated using the three-dimensional algorithm for ray tracing (bending). The computed data were perturbed with realistic noise to provide similar variance reduction as in the case of experimental inversion. Before starting recovery of the synthetic model, we "forgot" the origin times and coordinates of the sources. The recovery procedure follows the same steps and parameters as in the case of the experimental data. In particular, the processing starts with the preliminary source locations in the 1-D starting velocity model, which may provide strongly biased locations relevant to the "true" coordinates. Then, after several iterations of the velocity model recovering and source re-locations, the misfit in source coordinates gradually decreases.

In Figure 5, we present a traditional checkerboard test conducted to check the horizontal resolution. In the synthetic model, we define alternating positive and negative anomalies with amplitudes of ±7% that remain unchanged at all depths. Here we consider two cases with anomaly sizes of 30 × 30 km and 60 × 60 km. The *P* wave velocity model has slightly better resolution, mostly because of the larger number of the *P* wave data. For the smaller synthetic anomalies (left column in Figure 5), satisfactory resolution is achieved mostly in the central-northern part of the study area, where KNET stations were installed. In this area, the 30 km size patterns are robustly resolved to at least 25 km depth for both *P* and *S* wave models. In other parts of the study area, this size of anomalies is almost unresolvable. For the anomalies of 60 km in size (right column in Figure 5), the model is recovered in most parts of the study area for both *P* and *S* wave models. Based on this test, we can conclude that in the area of the KNET network, fair resolution is achieved, which allows us to robustly recover even smaller-scale patterns, whereas for the rest of the area, we can only resolve the general shapes of large structures.

The vertical resolution is explored in other tests with synthetic models associated with specific profiles. Because of the trade-off between the source depth and velocity distribution, the depth resolution is typically much poorer in cases of passive source tomography studies. In Figure 6, we present two tests associated to Profile 2 to present the main results. The checkerboard anomalies are defined along the vertical section. Across this section, the anomalies are defined within a band 100 km thick. In the first model, we evaluate anomalies with horizontal spacing of 50 km and depth spacing of 25 km. The first change of sign occurs at 10 km; it then changes at depths of 30 km, 55 km, etc. The resulting model shows fair recovering for the interface at 10 km depth, but it does not detect sign changes at 40 km and deeper. To further investigate the capacity of tomography to resolve deep interfaces, we created a second model with only one level of sign change at 30 km depth. In this case, the tomography reveals some changes of the anomaly sign at 30 km depth; however, the amplitudes of deeper anomalies are much weaker than those in the original model. All the resolution limitations identified in the synthetic tests should be considered when interpreting the inversion results of experimental data.

We have performed also a series of synthetic tests for the attenuation models. In this case, the workflow was much easier than during performing the tests for the velocity tomography. When computing the synthetic t^* and following recovering of the model, we used raypaths from fixed locations of sources. The inversion was performed within one step. In Figure 7, we present the results of the checkerboard tests for the *P* and *S* wave attenuation models. The lateral size of anomalies was 50 × 50 km; with depth, they remained unchanged. The synthetic t^* values were computed along actual raypaths, same as used in the experimental case. The calculated data were strongly perturbed by random noise providing the signal-to-noise level of approximately 0.8. The inversion of such data enabled relatively small variance reduction of around 20%, which was similar to that in the case of inversion of experimental data. Figure 7 shows that despite high noise level and low variance reduction, the anomalies of attenuation are well recovered in most parts of the study area.

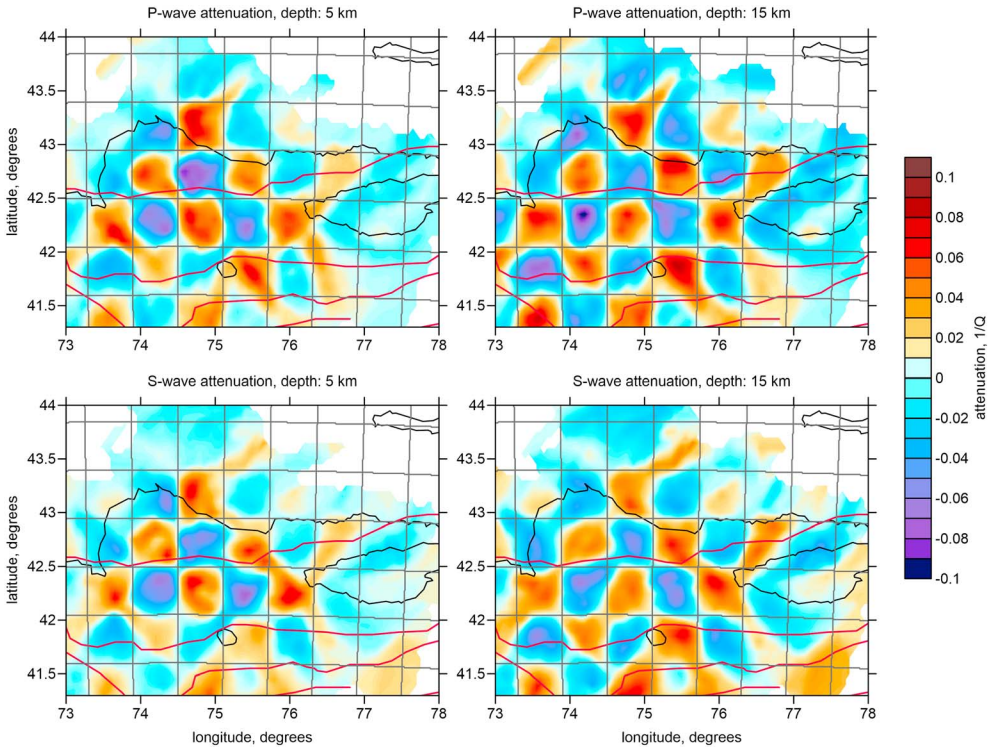

Figure 7. Checkerboard tests for the *P* and *S* wave attenuation models. The locations of the synthetic anomalies with the size of 50 × 50 km are highlighted with grey lines. The results are shown for the *P* and *S* wave attenuation models (upper and lower rows, respectively) for the depths of 5 and 15 km (left and right columns, respectively). The red lines depict the major faults.

Based on this test, we conclude that at least 50 km size can be resolved in both cases of the *P* and *S* wave attenuation data.

5. Tomography Results and Discussion

The results of *P* and *S* wave velocity anomalies derived from the iterative tomographic inversion are illustrated in horizontal sections (Figure 8) and vertical profiles (Figure 9). To facilitate interpretation, in the horizontal sections, we have added the main faults and topography. Here we mainly focus on the area of central-northern Kyrgyzstan, where the fair resolution is ensured by the dense ray coverage in the KNET network. For the rest of the study area, the results are similar to the model previously presented by Zabelina et al. (2013). In addition, Figure 10 shows the distributions of seismic attenuation of *P* and *S* waves at depths of 5 and 15 km.

The *P* and *S* velocity anomalies, which were computed independently, appear to be different in the shallow section, but in deeper sections, they appear almost identical. At 5 km depth, we observe that the *S* wave model exhibits a large high-velocity anomaly in the northern half of the study area, whereas in the *P* wave model, we observe alternation of the positive and negative anomalies. However, if we consider details within the high-velocity anomaly in the *S* model, similar structures to those in the *P* model can be identified based on the relative decrease and increase of anomalies. The difference between the *P* and *S* wave anomalies at shallow depths can be explained by the effects of the variations in composition and fluid saturation, which affect *P* and *S* velocities differently.

Source locations are obtained iteratively using the 3-D velocity models derived in the previous iterations. In vertical sections (Figure 9), one can see that most of earthquakes tend to be located within "blue" patterns in shallow parts of the crust that might be associated with brittle rocks. The amount of earthquakes in large low-velocity anomalies is much smaller that may indicate that these parts are mostly ductile. Most of seismicity is concentrated in the upper crust. However, there are some segments with deeper earthquakes corresponding

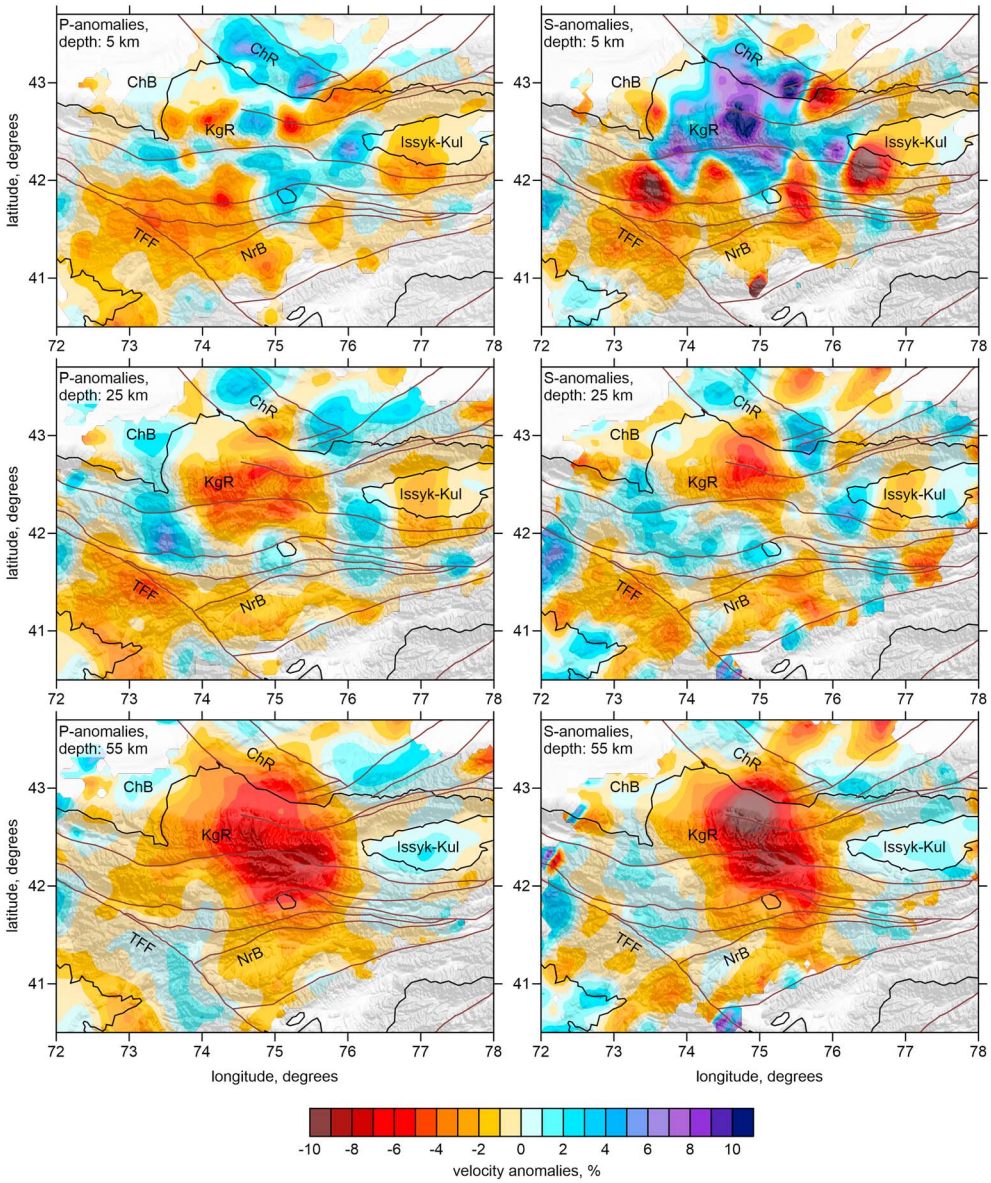

Figure 8. *P* and *S* wave velocity anomalies in horizontal sections. The brown lines depict the major faults. Background is the topography. Abbreviations: ChB, Chuya Basin (part of the Kazakh Plate); ChR, Chuya Ridge; KgR, Kyrgyz Range; TFF, Talas-Fergana Fault; NrB, Naryn Basin.

to the lower crust and uppermost mantle. Such events may be caused by deep penetration of brittle material due to collisional processes. However, some single deep events observed in sections might be related by instable location solutions due to noise in the data.

At shallow depths, the velocity structures seem to delineate the same structures as the major fault zones in the Tien Shan. For example, the large Talas-Fergana Fault zone is traced in *P* and *S* velocity anomalies at depths of 5 and 25 km, which indicates that this fault penetrates deep to the crust. The faults along the Naryn Basin are also associated with lower-velocity anomalies.

In the maps of *P* and *S* attenuation at depths of 5 and 15 km, the areas of higher attenuation are mostly associated with mountain areas, whereas the low-attenuation anomalies correspond to the stable segments of the Kazakh Shield. The depression of the Issyk Kul Lake is associated with a local decrease of attenuation in both the *P* and *S* wave attenuation models. A local increase of attenuation is also observed along the Chu Ridge, which separates the Chu Basin from the rest of the Kazakh Plate.

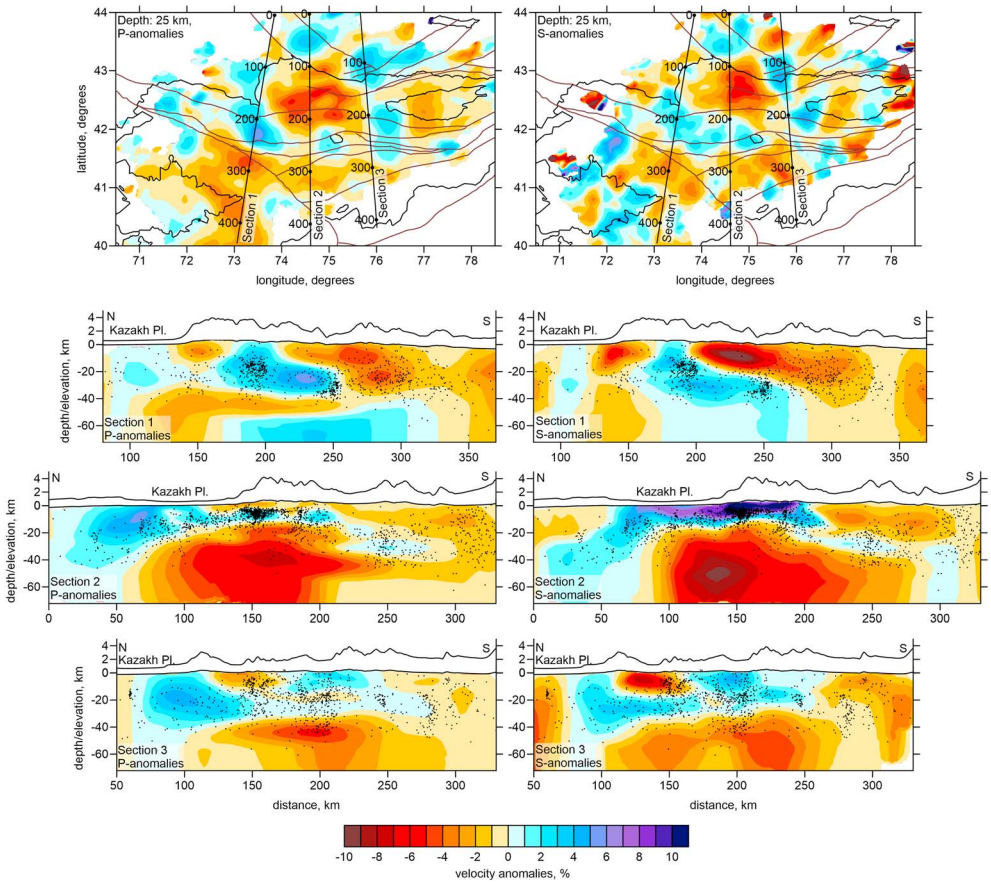

Figure 9. *P* and *S* wave velocity anomalies in vertical sections. The locations of the profiles are indicated in the maps in the upper part of the Figure. The projections of events located at distances of less than 40 km from the profile are indicated with black dots. The exaggerated topography along the profiles is shown above each section.

Because the *t** values for the *P* and *S* wave data were calculated independently, the observed good correlation of the *P* and *S* wave attenuation structures supports the robustness of the results. Indeed, strongly deformed and fractured crust in the mountainous areas strongly scatters seismic waves and, thus, similarly attenuates *P* and *S* wave s. In flat areas of the Kazakh Shield, this scattering is relatively minor, and the waves propagate with weak attenuation.

The attenuation models appear similar to the seismic velocity anomalies in the shallowest sections of the teleseismic study by Lei and Zhao (2007), which average the vertical properties of the entire crust. However, there is no direct correlation with our velocity models at shallow depths (Figure 8), which may be caused by differences in the sensitivity of the attenuation and velocity parameters to the effects of fracturing, composition, temperature, and fluid content. No apparent consistency is observed with another tomography model constructed for the same region by Xu et al. (2007). In respect to the model by Li et al. (2016), our results provide almost reverse shapes of anomalies: fast crustal velocities beneath the mountain areas and slow velocities the stable Kazakh Shield in Li et al. (2016) correspond to opposite anomalies in our results. On the contrary, our velocity and attenuation distributions in deep sections match with the Pn velocity distributions derived by Zhou and Lei (2015). Such strong differences between models produced by different authors may be caused by very strong complexity of the crustal structure and insufficient data coverage and quality.

Structures in the lower crust can be traced in the derived seismic velocity maps (Figure 8) and profiles (Figure 9). The most prominent feature of the velocity model is the negative anomaly located in the center of the study area, which is expressed similarly in both the *P* and *S* velocity distributions. As shown in Figure 11, this anomaly matches exactly with the area of thickest crust identified in the receiver function

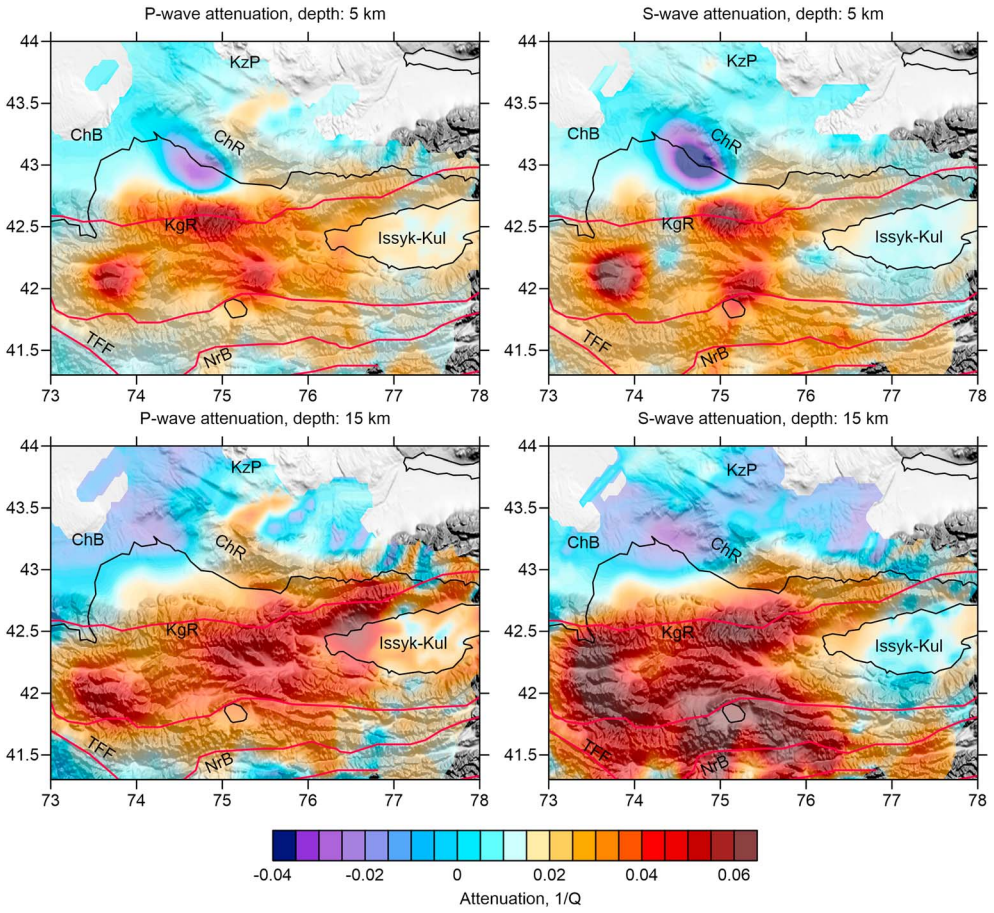

Figure 10. Deviations of the *P* and *S* wave velocity attenuation in horizontal sections. The red lines depict the major faults. Background is the topography. Abbreviations: ChB, Chuya Basin; KzP, Kazakh Plate; ChR, Chuya Ridge; KgR, Kyrgyz Range; TFF, Talas-Fergana Fault; NrB, Naryn Basin.

studies by Vinnik et al. (2004). Although seismic tomography represents continuous seismic heterogeneities and does not capture sharp contrasts of first-order interfaces, in some cases it may help identify depth variations of such strong interfaces like the Moho. For example, recent studies by Koulakov et al. (2015) and El Khrepy et al. (2016) have explicitly shown with experimental data and synthetic tests that velocity anomalies at depths corresponding to the average Moho depth do really represent variations of crustal thickness. Based on this finding, we propose that the prominent low-velocity anomaly observed in our results at deep sections corresponds to the local deepening of the Moho interface, as revealed by Vinnik et al. (2004). This area corresponds to the transition from the flat Kazakh Shield and the Kyrgyz Range, and its center does not correspond to the highest relief. Although this anomaly seem to not be fully isostatically compensated by relief, its location seems to correspond to the general tectonic settings of the Tien Shan region.

Based on the regional tomography model by Koulakov (2011) shown in Figure 12, the Tien Shan appears to be bounded by two thrust zones. To the south, we observe a large inclined high-velocity anomaly representing the northward dipping lithosphere of Tarim. To the north is a less prominent, but still visible, higher-velocity anomaly that may correspond to the underthrusted Kazakh lithosphere. In Figure 12, we also present the result of the crustal tomography produced in this study shown in the same profile. The low-velocity anomaly in the lower crust precisely matches with a zone where the Kazakh Plate dips underneath the Tien Shan. Such a collision process should cause the deepest Moho and considerable shortening of crustal material above the colliding plate.

One scenario for how this collision may occur in the collided partitions of the crust is presented in Figure 13. The rheology and strength distribution within the continental lithosphere have major implications on the

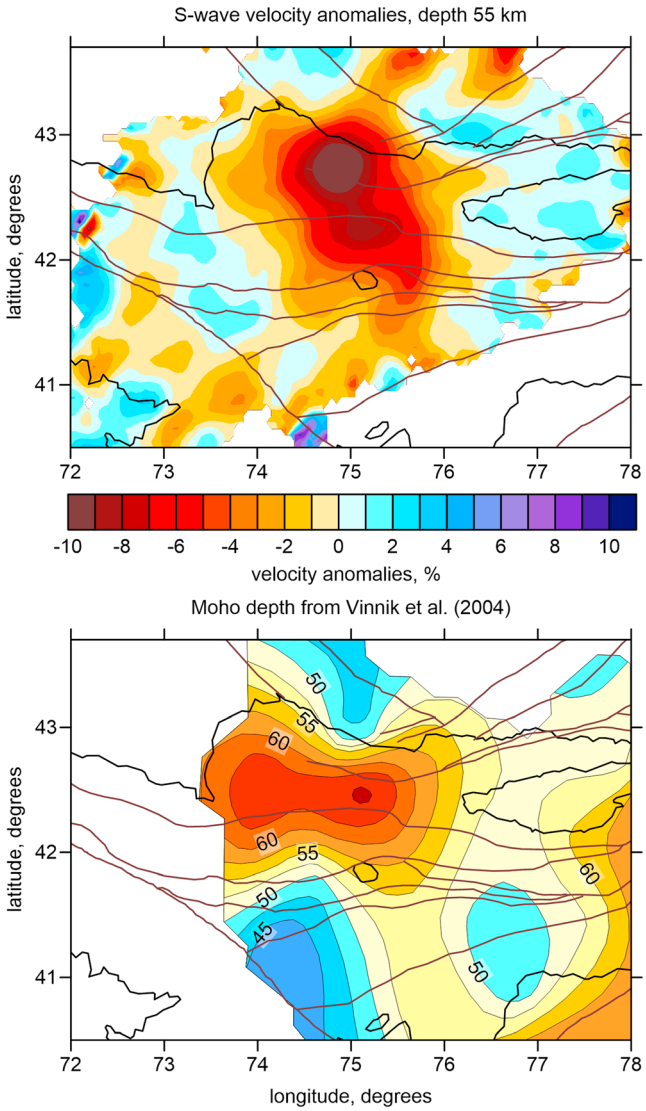

Figure 11. Comparison of the deep seismic velocity anomaly derived in this study with the Moho depth based on the receiver function study by Vinnik et al. (2004). The brown lines are the major faults. The numbers in the lower map indicate the Moho depth in kilometers.

behavior of the system during continental collision (e.g., Beaumont & Quinlan, 1994; Brun, 2002; Gray & Pysklywec, 2013; Vogt, Matenco, et al., 2017). The Brace–Goetze yield-stress envelopes (Brace & Kohlstedt, 1980; Goetze & Evans, 1979) show that the long-term strength of lithosphere varies as a function of depth according to the brittle and ductile deformation laws. For the continents, two end-member models of lithospheric strength ("crème brûlée" and "jelly sandwich") are commonly assumed (reviewed by Burov and Watts (2006) and Burov (2011)). In the crème brûlée model, the mantle is weak and strength is confined to the crust (e.g., Jackson, 2000; Maggi et al., 2000), whereas in the jelly sandwich model, strength resides in both the crust and the uppermost lithospheric mantle (e.g., Schmalholz et al., 2009; Watts & Burov, 2003). It is noteworthy that in contrast to brittle strength, which is largely rock-independent (Brace & Kohlstedt, 1980; Byerlee, 1978; Kohlstedt et al., 1995; Yamato & Brun, 2017), ductile rheology is strongly controlled by temperature and rock type. In particular, depending on the assumed flow law (e.g., Ranalli, 1995), the lower crust can either be "strong" (plagioclase) or "weak" (wet quartzite), which defines the degree of mechanical coupling between the rheological layers and the integrated strength of the lithosphere (Burov & Diament, 1995). As mentioned by Burov and Watts (2006), crème brûlée includes all models with a weak mantle, not just those with a weak lower crust. Therefore, a weak mantle model does not exclude a strong mafic lower crust (in case of stronger, e.g., plagioclase, ductile rheology). Such differences in the rheological profile may arise in the colliding plates experienced different history of tectonic and thermal development. Considerable strength contrasts between major continental plates have been reported by geological observation in different continent-continent collisional zones (e.g., Ziegler et al., 1995, 1998).

In the case of collision in the northern Tien Shan, both of these types of lithosphere may exist. Because the Kazakh Shield maintains high lithospheric mantle strength, it generally corresponds to the jelly sandwich case (left insert on Figure 13), whereas the lithosphere of the northern Tien Shan, which was strongly deformed in the Cenozoic Era, can be represented by the crème brûlée model with weak mantle lithosphere (right insert on Figure 13).

We propose that the relative seismic anomalies in the vertical section may represent vertical deviations of the crustal layers relative to their initial positions. If a layer ascends, the higher-velocity rocks appear at shallower depth and are therefore represented as high-velocity anomalies. However, the descending layer should appear in the vertical section with relative velocity deviations as a lower-velocity structure. Based on this assumption, we propose that the shallow high-velocity anomaly observed in the central part of section 2 (Figure 13) may represent the felsic part of the upper crust that ascended because of the collision. Note that most seismicity is observed within this high-velocity layer, which supports the inference of the brittle character of deformations in the upper crust.

In the right part of the section beneath the mountainous areas of the Tien Shan, we observe a less prominent, but still visible, positive anomaly at depths of around 20 km. Most seismicity seems to be associated with this layer. The assumption of a strong lower crust in the weak mantle model for the northern Tien Shan (see right insert on Figure 13) may explain its lateral penetration between the brittle upper and ductile lower crust (see left insert on Figure 13) of the Kazakh Plate. The abundant seismicity at 20–30 km depth in the right part of the section is also consistent with a strong lower crust in the Tien Shan segment. However, the low velocities in the central part of the section may be due to the relative descent of weak ductile lower crust of the Kazakh

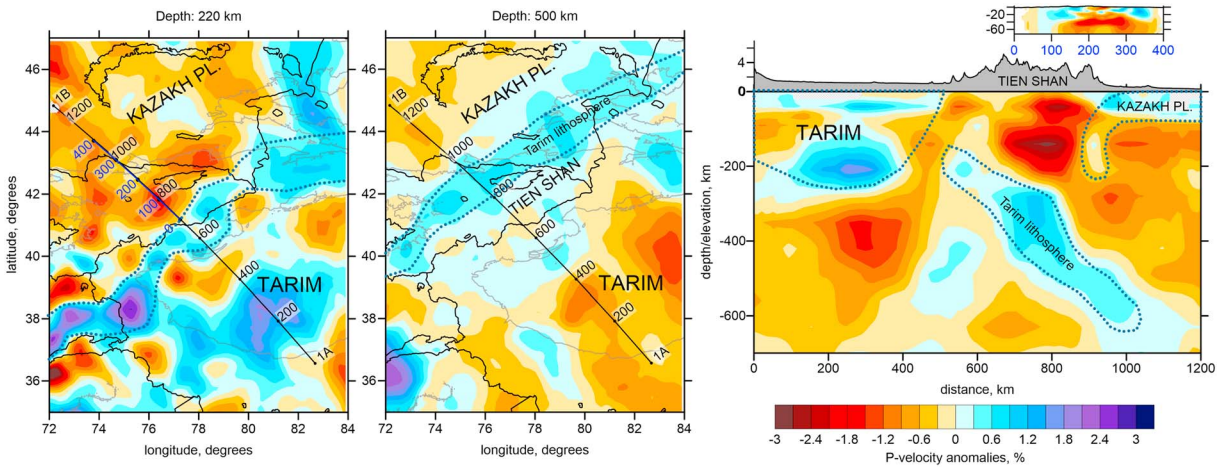

Figure 12. Geodynamic model of Tien Shan derived from the regional tomography study by Koulakov (2011). The maps to the left present the *P* wave velocity anomalies at the depths of 220 and 500 km. The light grey line indicates the contour of the relief altitude of 1,500 m. The dotted line indicates the possible location of the subducted Tarim lithosphere. Profile locations for the regional and local tomography results are presented. To the left, the vertical section of the regional is presented with possible shape of the Tarim lithosphere (dotted lines). The topography along the profile is indicated. In the upper corner, the result of the local tomography (this study) is presented in the vertical section with coordinated lateral location in respect to the regional profile.

Plate along the strong mantle lithosphere. According to our interpretation, the lower crust material may also detach from the mantle lithosphere and be accumulated in the accretionary wedge. The thickened crust behaves as a strong low-velocity anomaly relative to the higher-velocity mantle lithosphere located at the same depth. Such "crocodile" type structures that appear in continental collision zones due to layered rheology of the lithosphere have been reproduced in analogue (Midtkandal et al., 2013) and numerical (e.g., Vogt, Matenco, et al., 2017; Vogt, Willingshofer, et al., 2017) experiments describing realistic cases in Pyrenees, the New Zealand Apls, and the European Central Alps. Note that this scenario seems to be also consistent with the results of 3-D numerical modeling of continental collision by Gerya et al. (2008). The case shown in their Figure 12 may adequately represent the localized collision in an isolated area of the northern Tien Shan represented in our results.

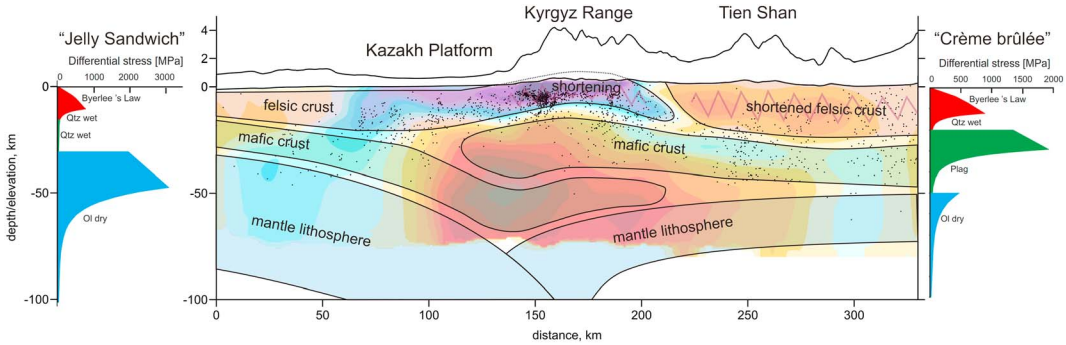

Figure 13. A cartoon showing possible interactions of crustal layers due to the collision of the Kazakh Plate with the Northern Tien Shan. Background is the *S* wave velocity model in section 2 (Same as in Figure 7). The dots are the earthquakes at distances of less than 40 km from the profile. The exaggerated relief along the profile is shown. The left and right inserts show Brace-Goetze failure envelopes for the collided Kazakh and Tien Shan plates. In the Northern Tien Shan, the strength is limited to the uppermost brittle layers of the upper and lower crust, and the lithospheric mantle is weak (the crème brûlée model—see, e.g., Jackson, 2000; Maggi et al., 2000). In the Kazakh Plate, the strength mainly resides in the brittle upper crust and mantle lithosphere separated by completely ductile lower crust (the jelly sandwich model—see, e.g., Burov & Watts, 2006; Schmalholz et al., 2009; Watts & Burov, 2003). For the upper crust and lithospheric mantle, wet quartzite (Qzt wet) and dry olivine (Ol dry) flow laws have been adopted. Note, however, that we assume the different lithology of the lower crust for the Kazakh Plate and the Northern Tien Shan: wet quartzite (Qzt wet) and plagioclase (Plag) flow laws, respectively. Strong lower crust in the weak mantle model for the Tien Shan segment explains its lateral penetration into weak lower crust of the Kazakh Plate and the abundant seismicity at 20–30 km depth in the right part of the section.

6. Conclusions

Based on the combined data set of the International KNET seismic network and the regional seismic data provided by the Institute of Seismology of Kyrgyzstan, we have constructed a 3-D model of crustal heterogeneities in *P* and *S* wave velocities beneath the northern Tien Shan. The large amount of data used in this study and thorough testing ensure high reliability and fair resolution of these results.

In addition, we present the first models of *P* and *S* seismic wave attenuation derived for this region. These models consistently show higher attenuation for the mountainous areas of the northern Tien Shan and lower attenuation for flat areas of the Kazakh Plate. The decrease of attenuation beneath the area of Issyk Kul Lake may indicate that it is located on a terrain with rigid, weakly deformed crust.

In the lower crust, the seismic velocity models show a prominent low-velocity anomaly located beneath the contact zone between the Kazakh Plate and the northern Tien Shan. It matches with existing receiver function data (Vinnik et al., 2004), which indicate the local dip of the Moho in this area. We propose that crustal thickening may be caused by underthrusting of the Kazakh Plate and formation of a thick accretionary complex in the crust.

The alternation of the higher and lower velocity layers in the vertical sections may be the result of a complex interaction between brittle and ductile crustal layers of the rheologically stratified Kazakh and Tien Shan plates. The existence of seismicity in only the upper high-velocity layer may indicate that the lithosphere of the Tien Shan plate in the collision zone behaves according to the crème brûlée rheological model (Burov & Watts, 2006).

Acknowledgments
This study was supported by the Russian Science Foundation grant 14-17-00430. N. Sycheva is supported by the RFBR project 15-05-06857a. The authors extend their appreciation to the International Scientific Partnership Program ISPP at King Saud University for funding this research through ISPP 0044. A. Koptev is supported by the Advanced ERC grant 290864 RHEOLITH. LOTOS code and velocity tomography model can be downloaded from http://www.ivan-art.com/temp/lotos_kyrgyz.zip.

References

Abdrakhmatov, K. E., Aldazhanov, S. A., Hager, B. H., Hamburger, M. W., Herring, T. A., Kalabaev, K. B., et al. (1996). Relatively recent construction of the Tien Shan inferred from GPS measurements of present-day crustal deformation rates. *Nature*, *384*(6608), 450–453. https://doi.org/10.1038/384450a0

Abdrakhmatov, K., Weldon, R. J., Thompson, S. C., Burbank, D. W., Rubin, C., Miller, M., & Molnar, P. (2001). Onset, style and current rate of shortening in the central Tien Shan, Kyrgyz Republic. *Russian Geology and Geophysics*, *42*(10), 1585–1609.

Batalev, V. Y., & Bataleva, E. A. (2013). The state of the lithosphere in the junction zone of Tarim and Tien Shan according to the petrological interpretation of the magnitotelluric data. *Izvestia. Physics of the Solid Earth*, *49*(3), 384–391. https://doi.org/10.1134/S1069351313030026

Batalev, V. Y., Bataleva, E. A., Egorova, V. V., Matyukov, V. E., & Rybin, A. K. (2011). The lithospheric structure of the Central and Southern Tien Shan: MTS data correlated with petrology and laboratory studies of lower-crust and upper-mantle xenoliths. *Russian Geology and Geophysics*, *52*(12), 1592–1599. https://doi.org/10.1016/j.rgg.2011.11.005

Beaumont, C., & Quinlan, G. (1994). A geodynamic framework for interpreting crustal-scale seismic-reflectivity patterns in compressional orogens. *Geophysical Journal International*, *116*(3), 754–783. https://doi.org/10.1111/j.1365-246X.1994.tb03295.x

Bielinski, R., Park, S., Rybin, A., Batalev, V., Jun, S., & Sears, C. (2003). Lithospheric heterogeneity in the Kyrgyz Tien Shan imaged by manetotelluric studies. *Geophysical Research Letters*, *30*(15), 1806. https://doi.org/10.1029/2003GL017455

Brace, W. F., & Kohlstedt, D. L. (1980). Limits on lithospheric stress imposed by laboratory experiments. *Journal of Geophysical Research*, *85*(B11), 6248–6252. https://doi.org/10.1029/JB085iB11p06248

Brun, J.-P. (2002). Deformation of the continental lithosphere: Insights from brittle-ductile models. *Geological Society, London, Special Publications*, *200*(1), 355–370. https://doi.org/10.1144/GSL.SP.2001.200.01.20

Brune, J. N. (1970). Tectonic stress and the spectra of seismic shear waves from earthquakes. *Journal of Geophysical Research*, *75*(26), 4997–5009. https://doi.org/10.1029/JB075i026p04997

Burov, E. B. (2011). Rheology and strength of the lithosphere. *Marine and Petroleum Geology*, *28*(8), 1402–1443. https://doi.org/10.1016/j.marpetgeo.2011.05.008

Burov, E. B., & Diament, M. (1995). The effective elastic thickness (Te) of continental lithosphere: What does it really mean? *Journal of Geophysical Research*, *100*(B3), 3905–3927. https://doi.org/10.1029/94JB02770

Burov, E. B., & Watts, A. B. (2006). The long-term strength of continental lithosphere: "Jelly sandwich" or "crème brûlée"? *GSA Today*, *16*(1), 4. https://doi.org/10.1130/1052-5173(2006)016%3C4:TLTSOC%3E2.0.CO;2

Buslov, M. M., De Grave, J., & Bataleva, E. A. (2004). Cenozoic tectonics and geodynamic evolution of the Tien Shan mountain belt as response to India-Eurasia convergence. *Himalayan Journal of Sciences*, *2*(4), 106–107.

Byerlee, J. (1978). Friction of rocks. *Pure and Applied Geophysics*, *116*(4-5), 615–626. https://doi.org/10.1007/BF00876528

Chen, Y., Roecker, S., & Kosarev, G. (1997). Elevation of the 410 km discontinuity beneath the central Tien Shan: Evidence for a detached lithospheric root. *Geophysical Research Letters*, *24*(12), 1531–1534. https://doi.org/10.1029/97GL01434

El Khrepy, S., Koulakov, I., Al-Arifi, N., & Petrunin, A. (2016). Seismic structure beneath the Gulf of Aqaba and adjacent areas based on the tomographic inversion of regional earthquake data. *Solid Earth*, *7*(3), 965–978. https://doi.org/10.5194/se-7-965-2016

Gamburtsev, G. A. (1960). Deep seismic sounding of the Earth's crust in the northern Tien Shan. In *Selected Works* [in Russian] (316 pp.). Izd. AN SSSR, Moscow.

Gerya, T. V., Perchuk, L. L., & Burg, J. P. (2008). Transient hot channels: Perpetrating and regurgitating ultrahigh-pressure, high-temperature crust–mantle associations in collision belts. *Lithos*, *103*(1-2), 236–256. https://doi.org/10.1016/j.lithos.2007.09.017

Ghose, S., Hamburger, M., & Virieux, J. (1998). Three-dimensional velocity structure and earthquake locations beneath the northern Tien Shan of Kyrgyzstan, central Asia. *Journal of Geophysical Research*, *103*(B2), 2725–2748. https://doi.org/10.1029/97JB01798

Goetze, C., & Evans, B. (1979). Stress and temperature in the bending lithosphere as constrained by experimental rock mechanics. *Geophysical Journal International*, *59*(3), 463–478. https://doi.org/10.1111/j.1365-246X.1979.tb02567.x

Gray, R., & Pysklywec, R. N. (2013). Influence of viscosity pressure dependence on deep lithospheric tectonics during continental collision. *Journal of Geophysical Research: Solid Earth*, *118*, 3264–3273. https://doi.org/10.1002/jgrb.50220

Haberland, C., & Rietbrock, A. (2001). Attenuation tomography in the western central Andes: A detailed insight into the structure of a magmatic arc. *Journal of Geophysical Research*, *106*(B6), 11,151–11,167. https://doi.org/10.1029/2000JB900472

Jackson, J. A. (2000). Strength of the continental lithosphere: Time to abandon the jelly sandwich? *GSA Today*, *12*, 4–10.

Kohlstedt, D. L., Evans, B., & Mackwell, S. J. (1995). Strength of the lithosphere: Constraints imposed by laboratory experiments. *Journal of Geophysical Research*, *100*(B9), 17,587–17,602. https://doi.org/10.1029/95JB01460

Kosarev, G., Petersen, N., & Vinnik, L. (1993). Receiver functions for the Tien Shan analog broadband network: Contrasts in the evolution of structures across the Talasso-Fergana fault. *Journal of Geophysical Research*, *98*(B3), 4437–4448. https://doi.org/10.1029/92JB02651

Koulakov, I. (2009). LOTOS code for local earthquake tomographic inversion: Benchmarks for testing tomographic algorithms. *Bulletin of the Seismological Society of America*, *99*(1), 194–214. https://doi.org/10.1785/0120080013

Koulakov, I. (2011). High-frequency *P* and *S* velocity anomalies in the upper mantle beneath Asia from inversion of worldwide traveltime data. *Journal of Geophysical Research*, *116*, B04301. https://doi.org/10.1029/2010JB007938

Koulakov, I., Bindi, D., Parolai, S., Grosser, H., & Milkereit, C. (2010). Distribution of seismic velocities and attenuation in the crust beneath the north Anatolian Fault (Turkey) from local earthquake tomography. *Bulletin of Seismological Society of America*, *100*(1), 207–224. https://doi.org/10.1785/0120090105

Koulakov, I., Maksotova, G., Mukhopadhyay, S., Raoof, J., Kayal, J. R., Jakovlev, A., & Vasilevsky, A. N. (2015). Variations of the crustal thickness in Nepal Himalayas based of tomographic inversion of regional earthquake data. *Solid Earth*, *6*(1), 207–216. https://doi.org/10.5194/se-6-207-2015

Larson, K. M., Bürgmann, R., Bilham, R., & Freymueller, J. T. (1999). Kinematics of the India-Eurasia collision zone from GPS measurements. *Journal of Geophysical Research*, *104*(B1), 1077–1093. https://doi.org/10.1029/1998JB900043

Lei, J. (2011). Seismic tomographic imaging of the crust and upper mantle under the central and western Tien Shan orogenic belt. *Journal of Geophysical Research*, *116*, B09305. https://doi.org/10.1029/2010JB008000

Lei, J., & Zhao, D. (2007). Teleseismic *P* wave tomography and the upper mantle structure of the central Tien Shan orogenic belt. *Physics of the Earth and Planetary Interiors*, *162*(3-4), 165–185. https://doi.org/10.1016/j.pepi.2007.04.010

Li, Z., Roecker, S., Li, Z., Wei, B., Wang, H., Schelochkov, G., & Bragin, V. (2009). Tomographic images of the crust and upper mantle beneath the western Tien Shan from the MANAS broadband deployment: Possible evidence for lithospheric delamination. *Tectonophysics*, *477*(1-2), 49–57. https://doi.org/10.1016/j.tecto.2009.05.007

Li, Y., Shi, L., & Gao, J. (2016). Lithospheric structure across the central Tien Shan constrained by gravity anomalies and joint inversions of receiver function and Rayleigh wave dispersion. *Journal of Asian Earth Sciences*, *124*, 191–203. https://doi.org/10.1016/j.jseaes.2016.05.003

Maggi, A., Jackson, J. A., McKenzie, D., & Priestley, K. (2000). Earthquake focal depths, effective elastic thickness, and the strength of the continental lithosphere. *Geology*, *28*(6), 495–498. https://doi.org/10.1130/0091-7613(2000)28%3C495:EFDEET%3E2.0.CO;2

Makarov, V. I., Alekseev, D. V., Batalev, V. Y., Bataleva, E. A., Belyaev, I. V., Bragin, V. D., et al. (2010). Underthrusting of Tarim beneath the Tien Shan and deep structure of their junction zone: Main results of seismic experiment along MANAS profile Kashgar-Song-Köl. *Geotektonika*, *44*(2), 102–126. https://doi.org/10.1134/S0016852110020020

Midtkandal, I., Brun, J. P., Gabrielsen, R. H., & Huismans, R. S. (2013). Control of lithosphere rheology on subduction polarity at initiation: Insights from 3D analogue modelling. *Earth and Planetary Science Letters*, *361*, 219–228. https://doi.org/10.1016/j.epsl.2012.10.026

Molnar, P., & Tapponnier, P. (1975). Cenozoic tectonics of Asia: Effects of a continental collision. *Science*, *189*(4201), 419–426. https://doi.org/10.1126/science.189.4201.419

Nolet, G. (1987). Seismic wave propagation and seismic tomography. In G. Nolet (Ed.), *Seismic Tomography*, (pp. 1–23). Dordrecht: Reidel. https://doi.org/10.1007/978-94-009-3899-1_1

Omuralieva, A., Nakajima, J., & Hasegawa, A. (2009). Three-dimensional seismic velocity structure of the crust beneath the central Tien Shan, Kyrgyzstan: Implications for large- and small-scale mountain building. *Tectonophysics*, *465*(1-4), 30–44. https://doi.org/10.1016/j.tecto.2008.10.010

Oreshin, S., Vinnik, L., Peregoudov, D., & Roecker, S. (2002). Lithosphere and asthenosphere of the Tien Shan imaged by *S* receiver functions. *Geophysical Research Letters*, *29*(8), 1191. https://doi.org/10.1029/2001GL014441

Paige, C. C., & Saunders, M. A. (1982). LSQR: An algorithm for sparse linear equations and sparse least squares. *ACM Transactions on Mathematical Software*, *8*(1), 43–71. https://doi.org/10.1145/355984.355989

Ranalli, G. (1995). *Rheology of the Earth*, (second ed.p. 413). London: Chapman and Hall.

Rietbrock, A. (2001). P wave attenuation structure in the fault area of the 1995 Kobe earthquake. *Journal of Geophysical Research*, *106*(B3), 4141–4154. https://doi.org/10.1029/2000JB900234

Roecker, S., Sabitova, T., Vinnik, L., Burmakov, Y., Golvanov, M., Mamatkanova, R., & Munirova, L. (1993). Three-dimensional elastic wave velocity structure of the western and central Tien Shan. *Journal of Geophysical Research*, *98*(B9), 15,779–15,795. https://doi.org/10.1029/93JB01560

Rybin, A. K., (2010). Magnetotelluric and seismic researches along the transect MANAS, *Vestnik VGU, Series Geology*, *1*, 218–228.

Sabitova, T. M., & Adamova, A. A. (2001). Seismic tomography study of the Tien Shan crust (results, problems, and prospects). *Geologiya i Geofizika (Russian Geology and Geophysics)*, *42*(10), 1543–1553.

Sabitova, T. M., Lesik, O. M., & Adamova, A. A. (1998). Velocity and density heterogeneities of the Tien-Shan lithosphere. *Pure and Applied Geophysics*, *151*(2-4), 539–548. https://doi.org/10.1007/s000240050128

Schmalholz, S. M., Kaus, B. J. P., & Burg, J.-P. (2009). Stress-strength relationship in the lithosphere during continental collision. *Geology*, *37*(9), 775–778. https://doi.org/10.1130/G25678A.1

Sychev, I., Koulakov, I., El Khrepy, S., & Al-Arifi, N. (2017). Pathways of volatile migration in the crust beneath Harrat Lunayyir (Saudi Arabia) during the unrest in 2009 revealed by attenuation tomography. *Journal of Volcanology and Geothermal Research*, *330*, 1–13. https://doi.org/10.1016/j.jvolgeores.2016.12.002

Tapponnier, P., & Molnar, P. (1979). Active faulting and Cenozoic tectonics of the Tien Shan, Mongolia, and Baikal regions. *Journal of Geophysical Research*, *84*(B7), 3425–3459. https://doi.org/10.1029/JB084iB07p03425

Tian, X., Zhao, D., Zhang, H., Tian, Y., & Zhang, Z. (2010). Mantle transition zone topography and structure beneath the central Tien Shan orogenic belt. *Journal of Geophysical Research*, *115*, B10308. https://doi.org/10.1029/2008JB006229

Um, J., & Thurber, C. H. (1987). A fast algorithm for two-point seismic ray tracing. *Bulletin of the Seismological Society of America*, *77*, 972–986.

Vinnik, L., Reigber, C., Aleshin, I., Kosarev, G., Kaban, M., Oreshin, S., & Roecker, S. (2004). Receiver function tomography of the central Tien Shan. *Earth and Planetary Science Letters*, *225*(1-2), 131–146. https://doi.org/10.1016/j.epsl.2004.05.039

Vinnik, L. P., Roecker, S., Kosarev, G. L., Oreshin, S. I., & Koulakov, I. Y. (2002). Crustal structure and dynamics of the Tien Shan. *Geophysical Research Letters*, *29*(22), 2047. https://doi.org/10.1029/2002GL015531

Vogt, K., Matenco, L., & Cloetingh, S. (2017). Crustal mechanics control the geometry of mountain belts. Insights from numerical modelling. *Earth and Planetary Science Letters*, *460*, 12–21. https://doi.org/10.1016/j.epsl.2016.11.016

Vogt, K., Willingshofer, E., Matenco, L., Sokoutis, D., Gerya, T., & Cloetingh, S. (2017). The role of lateral strength contrasts in orogenesis: A 2D numerical study. *Tectonophysics*. https://doi.org/10.1016/j.tecto.2017.08.010

Watts, A. B., & Burov, E. B. (2003). Lithospheric strength and its relationship to the elastic and seismogenic layer thickness. *Earth and Planetary Science Letters*, *213*(1-2), 113–131. https://doi.org/10.1016/S0012-821X(03)00289-9

Xu, Y., Li, Z., & Roecker, S. (2007). Uppermost mantle structure and its relation with seismic activity in the central Tien Shan. *Geophysical Research Letters*, *34*, L10304. https://doi.org/10.1029/2007GL029708

Yamato, P., & Brun, J. P. (2017). Metamorphic record of catastrophic pressure drops in subduction zones. *Nature Geoscience*, *10*(1), 46–50. https://doi.org/10.1038/ngeo2852

Yu, Y., Zhao, D., & Lei, J. (2017). Mantle transition zone discontinuities beneath the Tien Shan. *Geophysical Journal International*, *211*(1), 80–92. https://doi.org/10.1093/gji/ggx287

Zabelina, I., Koulakov, I., & Buslov, M. M. (2013). Deep mechanisms in the Kyrgyz Tien Shan orogen (from results of seismic tomography). *Russian Geology and Geophysics*, *54*(7), 695–706. https://doi.org/10.1016/j.rgg.2013.06.005

Zhao, J., Liu, G., Lu, Z., Zhang, X., & Zhao, G. (2003). Lithospheric structure and dynamic processes of the Tianshan orogenic belt and the Junggar basin. *Tectonophysics*, *376*(3-4), 199–239. :https://doi.org/10.1016/j.tecto.2003.07.001

Zhou, Z., & Lei, J. (2015). Pn anisotropic tomography under the entire Tienshan orogenic belt. *Journal of Asian Earth Sciences*, *111*, 568–579. https://doi.org/10.1016/j.jseaes.2015.06.009

Ziegler, P. A., Cloetingh, S., & van Wees, J. D. (1995). Dynamics of intra-plate compressional deformation: The Alpine foreland and other examples. *Tectonophysics*, *252*(1-4), 7–59. https://doi.org/10.1016/0040-1951(95)00102-6

Ziegler, P. A., Van Wees, J. D., & Cloetingh, S. (1998). Mechanical controls on collision-related compressional intraplate deformation. *Tectonophysics*, *300*(1-4), 103–129. https://doi.org/10.1016/S0040-1951(98)00236-4